

An Opacity-Free Method of Testing the Cosmic Distance Duality Relation Using Strongly Lensed Gravitational Wave Signals

Shun-Jia Huang,^{1,2,*} En-Kun Li,^{2,†} Jian-dong Zhang,² Xian Chen,^{3,4} Zucheng Gao,⁵ Xin-yi Lin,² and Yi-Ming Hu^{2,‡}

¹*School of Science, Shenzhen Campus of Sun Yat-sen University, Shenzhen 518107, China*
²*MOE Key Laboratory of TianQin Mission, TianQin Research Center for Gravitational Physics & School of Physics and Astronomy, Frontiers Science Center for TianQin, Gravitational Wave Research Center of CNSA, Sun Yat-sen University (Zhuhai Campus), Zhuhai 519082, China*
³*Astronomy Department, School of Physics, Peking University, Beijing 100871, China*
⁴*Kavli Institute for Astronomy and Astrophysics, Peking University, Beijing 100871, China*
⁵*Institute of Astronomy, University of Cambridge, Madingley Road, Cambridge CB3 0HA, UK*

(Dated: February 28, 2024)

The cosmic distance duality relation (CDDR), expressed as $D_L(z) = (1+z)^2 D_A(z)$, plays an important role in modern cosmology. In this paper, we propose a new method of testing CDDR using strongly lensed gravitational wave (SLGW) signals. Under the geometric optics approximation, we calculate the gravitational lens effects of two lens models, the point mass and singular isothermal sphere. We use functions of $\eta_1(z) = 1 + \eta_0 z$ and $\eta_2(z) = 1 + \eta_0 z / (1+z)$ to parameterize the deviation of CDDR. By reparameterizing the SLGW waveform with CDDR and the distance-redshift relation, we include the deviation parameters η_0 of CDDR as waveform parameters. We evaluate the ability of this method by calculating the parameter estimation of simulated SLGW signals from massive binary black holes. We apply the Fisher information matrix and Markov Chain Monte Carlo methods to calculate parameter estimation. We find that with only one SLGW signal, the measurement precision of η_0 can reach a considerable level of 0.5-1.3% for $\eta_1(z)$ and 1.1-2.6% for $\eta_2(z)$, depending on the lens model and parameters.

arXiv:2402.17349v1 [astro-ph.CO] 27 Feb 2024

* corresponding author: huangshj9@mail2.sysu.edu.cn

† corresponding author: lienk@mail.sysu.edu.cn

‡ corresponding author: huyiming@sysu.edu.cn

CONTENTS

I. Introduction	2
II. Test CDDR with strongly lensed gravitational wave (SLGW) signals	3
III. Parameter estimation methods	5
IV. Results	6
V. Summary and discussion	10
Acknowledgments	12
A. Coordinate transformation	13
References	13

I. INTRODUCTION

The research of modern cosmology heavily relies on the measurement of celestial distances, such as the angular diameter distance $D_A(z)$ and the luminosity distance $D_L(z)$. The cosmic distance duality relation (CDDR), as a fundamental relation in modern cosmology, establishes a connection between $D_A(z)$ and $D_L(z)$, that is $D_L(z) = (1+z)^2 D_A(z)$ [1, 2]. The CDDR holds if the spacetime is described by a metric theory of gravity, as long as photons travel along null geodesics, and the photon number is conserved during propagation [1, 2]. Testing the validity of CDDR can not only deepen our understanding of the universe but also reveal new physical or astrophysical mechanisms [3–5]. Additionally, the CDDR, serving as a fundamental relation in cosmology, finds extensive applications in diverse astronomical research. These include studies related to the measurements of cosmic curvature through strong gravitational lensing (SGL) systems [6–8], the observations of the large-scale distribution of galaxies and the near-uniformity of the cosmic microwave background radiation temperature [9], as well as investigations into the geometrical shape, gas mass density profile, and temperature profile of galaxy clusters [10–12].

The idea of testing CDDR is simple, just measure $D_A(z)$ and $D_L(z)$ at the same redshift, and then compare these two distances to see whether CDDR is valid or not. Numerous studies have focused on testing CDDR using diverse observational datasets (see [13–27] and the references therein). Type Ia supernovae (SNe Ia) are considered excellent standard candles and are extensively employed for $D_L(z)$ measurements. Conversely, $D_A(z)$ is typically derived from a variety of observations such as the Sunyaev-Zeldovich effect of galaxy clusters and the gas mass fraction measurements in galaxy clusters [13–16], the baryon acoustic oscillations (BAO) [17], the SGL systems [18, 19], and the angular size of ultra-compact radio (UCR) sources [20]. For instance, combining $D_A(z)$ obtained from galaxy clusters with SNe Ia provides a means to test CDDR [13–16]. A new model-independent cosmological test for the CDDR was carried out by Xu et al. [21], combining the latest five BAO measurements and the Pantheon SNe Ia sample. A model-independent methodology employing SGL systems and SNe Ia to test CDDR was proposed by Liao et al. [22]. However, the redshift limitation of SNe Ia renders SGL systems with a source redshift greater than 1.4 impractical for CDDR testing, as there are no SNe Ia that correspond to these SGL systems at the same redshift. Consequently, the available data pairs are significantly fewer than the total number of SGL systems. To make use of the full SGL data to test CDDR, Tang et al. [23] reconstruct $D_L(z)$ from SNe Ia up to the highest redshift of SGL using deep learning. Liu et al. [24] present a new method to use the measurements of UCR sources and the latest observations of SNe Ia to test CDDR and use the Artificial Neural Network algorithm to reconstruct the possible evolution of CDDR with redshifts.

These traditional methods for testing CDDR have some limitations. Firstly, distance measurements based on electromagnetic (EM) wave observations are affected by the cosmic opacity [28–30]. Secondly, it is necessary to assume that the universe is isotropic because these traditional methods measure distances from different objects located at different redshifts and directions, and then use techniques such as interpolation to test CDDR [31]. With the implementation of gravitational wave (GW) detection [32–36], we are now in the era of GW astronomy and cosmological research [37, 38]. Recently, a new method has been discovered that testing CDDR using simulated SLGW signals based on the third-generation ground-based GW detector can avoid these limitations faced by traditional methods [25–27]. This is because the propagation of GW signals is not affected by the cosmic opacity and can directly measure $D_L(z)$. Additionally, if the time delay between the double images of SLGW and EM observation including

the Einstein angle and the velocity dispersion of the SGL galaxy are available, $D_A(z)$ to the same object unaffected by the cosmic opacity can be measured.

Future space-based GW detectors are also expected to detect SLGW signals [39, 40]. TianQin is a planned space-based GW observatory designed for sensitivity in the millihertz band [41]. In recent years, considerable efforts have been dedicated to examining and consolidating the scientific potential of TianQin [42–71]. Concerning detected GW sources, TianQin’s sky localization precision can achieve a range from 1 deg² to 0.1 deg² [46–49], enabling the potential integration of subsequent EM observations for multi-messenger astronomy. An effective way to obtain the redshift is from the EM counterparts. For example, If the massive binary black hole (MBBH) evolve in a gas-rich environment, the gas will be absorbed into the massive black hole (MBH), which will generate EM radiation across all band [72]. As long as the sky localization precision provided by the GW signal is good enough, there will be opportunities to realize the detection of EM counterparts [73]. For a rough estimation of the SLGW detection rate, we consider a detection probability of SLGW resulting from MBBH mergers as approximately 1% for space-based GW detectors [40]. Under an optimistic model, the detection rate of GW from MBBH is estimated to be $\gtrsim O(10^2)/yr$ [46]. Consequently, the total number of detected SLGW events could be as high as $\gtrsim O(5)$ over the five-year mission lifetime.

In this paper, we propose a new method of testing CDDR using SLGW signals. By reparameterizing the SLGW waveform with CDDR and the distance-redshift relation, we include the deviation parameters of CDDR as waveform parameters. In this way, measurements based on SLGW signals can directly constrain the deviation parameters and test CDDR. We assess the ability of this novel method in testing CDDR and present preliminary results for TianQin. We considered MBBHs as GW sources, allowing the potential extension of the redshift range for testing CDDR to values significantly greater than the limit imposed by SNe Ia observations, which is 1.4. This new method requires additional EM information on the redshifts of the source and lens to test CDDR.

This paper is organized as follows. In Section II, we describe a new method to test CDDR using SLGW signals. In Section III, we introduce the parameter estimation method used in this study. In Section IV, we evaluate the ability to test CDDR using SLGW signals. Finally, we summarize and discuss in Section V. Throughout this paper, we use $G = c = 1$ and assume a flat Λ CDM cosmology with the parameters $\Omega_M = 0.315$, $\Omega_\Lambda = 0.685$ and $H_0 = 67.66 \text{ km s}^{-1} \text{ Mpc}^{-1}$ [9].

II. TEST CDDR WITH SLGW SIGNALS

When the Schwarzschild radius, $R_S \equiv 2GM_L/c^2$, of the gravitational lens is much larger than the wavelength of GW¹, the wave effect can be neglected and geometric optics approximation (GOA) can be applied. Under the GOA, considering the point mass (PM) and Singular Isothermal Sphere (SIS) lens model, the SLGW has two images. The observed SLGW signals are given in the stationary phase approximation as [65, 74],

$$\begin{aligned} \tilde{h}^L(f) = & \left[|\mu_+|^{1/2} \Lambda(t) e^{-i(\phi_D + \phi_p)(t(f))} \right. \\ & \left. - i |\mu_-|^{1/2} e^{2\pi i f t_d} \Lambda(t(f) + t_d) e^{-i(\phi_D + \phi_p)(t(f) + t_d)} \right] \\ & \times \mathcal{A} f^{-7/6} e^{i\Psi(f)}, \end{aligned} \quad (1)$$

where the GW amplitude and phase are

$$\mathcal{A} = \sqrt{\frac{5}{96}} \frac{\pi^{-2/3} \mathcal{M}_z^{5/6}}{D_L^S} \quad (2)$$

and

$$\Psi(f) = 2\pi f t_c - \phi_c - \frac{\pi}{4} + \psi_{\text{PN}}. \quad (3)$$

In the above expression, D_L^S is the luminosity distance to the GW source, t_c and ϕ_c are coalescence time and phase, respectively. ψ_{PN} is the post-Newtonian (PN) phase as a function of the redshifted chirp mass $\mathcal{M}_z = (1 + z_S)(M_1 M_2)^{3/5} / (M_1 + M_2)^{1/5}$ and symmetric mass ratio $\eta = (M_1 M_2) / (M_1 + M_2)^2$, where M_1 and M_2 are binary

¹ This condition can also be expressed as $M_L \gg 10^8 M_\odot (f/\text{mHz})^{-1}$.

masses. In this work, we expand the PN phase and $t(f)$ to 2 PN order (see [43] and the references therein). The detector response, the polarization phase, and the Doppler phase can be defined by

$$\Lambda(t) = \sqrt{(1 + \cos^2 \iota)^2 F^+(t)^2 + 4 \cos^2 \iota F^\times(t)^2}, \quad (4)$$

$$\phi_P(t) = \tan^{-1} \left[\frac{2 \cos \iota F^\times(t)}{(1 + \cos^2 \iota) F^+(t)} \right], \quad (5)$$

and

$$\phi_D(t) = 2\pi f R \sin \left(\frac{\pi}{2} - \beta \right) \cos(2\pi f_m t - \lambda), \quad (6)$$

where $R = 1$ AU, $f_m = 1/\text{year}$ and ι is inclination angle. $F^{+, \times}(t)$ is the antenna pattern functions of the source's detector coordinates (θ_S, ϕ_S) and polarization angle ψ_S , and related to the motion and pointing of the detector. The antenna pattern functions are given by

$$\begin{aligned} F^+(t, \theta_S, \phi_S, \psi_S) &= \frac{\sqrt{3}}{2} \left[\frac{1}{2} (1 + \cos^2 \theta_S) \cos 2\phi_S \cos 2\psi_S - \cos \theta_S \sin 2\phi_S \sin 2\psi_S \right], \\ F^\times(t, \theta_S, \phi_S, \psi_S) &= \frac{\sqrt{3}}{2} \left[\frac{1}{2} (1 + \cos^2 \theta_S) \cos 2\phi_S \sin 2\psi_S + \cos \theta_S \sin 2\phi_S \cos 2\psi_S \right]. \end{aligned} \quad (7)$$

where the factor of $\sqrt{3}/2$ comes from the response change from a 90-degree laser interferometer to a 60-degree laser interferometer and $\phi_S(t) = \phi_{S0} + \omega t$ with $\omega \approx 2 \times 10^{-5}$ rad/s being the angular frequency of the TianQin satellites. The transformation from the source's ecliptic coordinates (β, λ) to the source's detector coordinates for TianQin can be found in Appendix A.

For the PM lens model used for lensing by compact objects such as black holes or stars, the magnification factor of each image and the time delay between the double images in Eq. (1) are given by [74]

$$\mu_{\pm} = \frac{1}{2} \pm \frac{y^2 + 2}{2y\sqrt{y^2 + 4}} \quad (8)$$

and

$$t_d = 4M_L(1 + z_L) \left[\frac{y\sqrt{y^2 + 4}}{2} + \ln \left(\frac{\sqrt{y^2 + 4} + y}{\sqrt{y^2 + 4} - y} \right) \right], \quad (9)$$

where $y = \eta_L / (2\sqrt{M_L}) \sqrt{D_A^L / (D_A^S D_A^{LS})}$ is the dimensionless source position in the lens plane, η_L , M_L and z_L are the GW source position in the lens plane, the lens mass and redshift, respectively. Here, D_A^L , D_A^S , and D_A^{LS} are the angular diameter distances to the lens, the source, and from the source to the lens, respectively.

For the SIS lens model used for more realistic lens objects than the PM lens, such as galaxies, stars cluster and dark matter halo, there are

$$\mu_{\pm} = \pm 1 + \frac{1}{y} \quad (10)$$

and

$$t_d = 8M_L(1 + z_L)y, \quad (11)$$

where $y = \eta_L / 4\pi v_d^2 D_A^{LS}$ and the lens mass inside the Einstein radius is given by $M_L = 4\pi^2 v_d^4 D_A^L D_A^{LS} / D_A^S$ in this case, and v_d is the velocity dispersion of lens galaxy. For this lens model, if $y \geq 1$, a single image of μ_+ is formed. For both PM and SIS lens models, when $y \rightarrow \infty$ ($\mu_+ = 1$ and $\mu_- = 0$), Eq. (1) reduces to the unlensed waveform.

In order to test any deviation from CDDR, we parameterize it with $(1 + z)^2 D_A / D_L = \eta(z)$ and Taylor-expand $\eta(z)$ in two ways (see [75–77] and the references therein):

(a) expand with redshift z , $\eta_1(z) = 1 + \eta_0 z$;

(b) expand with the scale factor $a = 1/(1 + z)$, $\eta_2(z) = 1 + \eta_0 z / (1 + z)$, which avoids divergences at high- z .

We reparameterize the SLGW waveform (Eq. (1)) and embed the CDDR in the waveform, which allows us to constrain the deviation of CDDR based on waveform analysis. Use the distance-redshift relationship [78]

$$D_A = \frac{1}{H_0(1+z)} \int_0^z dz' \frac{1}{E(z')}, \quad (12)$$

to reparameterize the angular diameter distance D_A^L , D_A^S , and D_A^{LS} , where $E(z) = \sqrt{\Omega_M(1+z)^3 + \Omega_K(1+z)^2 + \Omega_\Lambda}$ depicts the background evolution of the Universe. In this case, Eq. (1) can be rewritten as

$$\begin{aligned} \tilde{h}^L(f) = & \left[|\mu_+|^{1/2} \Lambda(t) e^{-i(\phi_D + \phi_p)(t)} \right. \\ & \left. - i |\mu_-|^{1/2} e^{2\pi i f t_d} \Lambda(t + t_d) e^{-i(\phi_D + \phi_p)(t + t_d)} \right] \\ & \times \sqrt{\frac{5}{96}} \frac{\pi^{-2/3} \mathcal{M}_z^{5/6}}{D_A^S(z_S)(1+z_S)^2 \eta(z_S)} f^{-7/6} e^{i\Psi(f)}. \end{aligned} \quad (13)$$

Assuming a flat Λ CDM model, we can describe a lensed waveform according to the above formulas with a set of 13 parameters: the lens mass M_L (for PM lens model) or velocity dispersion v_d (for SIS lens model), lens redshift z_L , GW source position in the lens plane η_L , deviation parameter of CDDR η_0 , GW source redshift z_S , redshifted chirp mass \mathcal{M}_z , symmetric mass ratio η , inclination angle ι , coalescence time t_c , coalescence phase ϕ_c , GW source ecliptic coordinates β , λ , and polarization angle ψ_S .

III. PARAMETER ESTIMATION METHODS

To evaluate the potential of measuring the Hubble constant using the SLGW signals, we apply both analytical and numerical methods with Fisher information matrix (FIM) and Markov Chain Monte Carlo (MCMC), respectively. Under the framework of Bayesian inference, one would like to constrain parameters θ with data d , or to obtain the posterior distribution $p(\theta|d, H)$ under model H . Under the Bayes' theorem,

$$p(\theta|d, H) = \frac{p(\theta|H)p(d|\theta, H)}{p(d|H)}, \quad (14)$$

the posterior is the product of the prior $p(\theta|H)$ and the likelihood $p(d|\theta, H)$, normalized by the evidence $p(d|H)$. The likelihood of the GW signal can be written as

$$p(d|\theta, H) \propto \exp \left[-\frac{1}{2} \left(d - h(\theta) \middle| d - h(\theta) \right) \right], \quad (15)$$

where the inner product $(\cdot|\cdot)$ defined as [79, 80]

$$(a|b) = 4\Re \int_0^\infty df \frac{\tilde{a}^*(f)\tilde{b}(f)}{\tilde{S}_n(f)}, \quad (16)$$

and $\tilde{S}_n(f)$ is the one-sided power spectral density, we adopt the formula from [49] for the expression of TianQin

$$\begin{aligned} \tilde{S}_n(f) = & \frac{1}{L^2} \left[\frac{4S_a}{(2\pi f)^4} \left(1 + \frac{10^{-4} Hz}{f} \right) + S_x \right] \\ & \times \left[1 + 0.6 \left(\frac{f}{f_*} \right)^2 \right], \end{aligned} \quad (17)$$

where $L = \sqrt{3} \times 10^5 \text{ km}$, $S_x = 1 \times 10^{-24} \text{ m}^2 \text{ Hz}^{-1}$, $S_a = 1 \times 10^{-30} \text{ m}^2 \text{ s}^{-4} \text{ Hz}^{-1}$, and $f_* = c/2\pi L$. In our case we consider the SLGW waveform $h(\theta)$ described by Eq. (13).

The FIM Γ_{ij} is defined as

$$\Gamma_{ij} = \left(\frac{\partial h}{\partial \theta_i} \middle| \frac{\partial h}{\partial \theta_j} \right), \quad (18)$$

where θ_i stands for the i -th GW parameter. In the limit that a signal is associated with a large signal-to-noise ratio (SNR) $\rho = \sqrt{(h|h)} \gg 1$, one can approximate the variance-covariance matrix with the inverse of the FIM $\Sigma = \Gamma^{-1}$, with Σ_{ii} describing the marginalized variances of the i -th parameter.

We adopt the emcee [81] implementation of the affine invariant MCMC sampler.

TABLE I. The parameter value and prior for SLGW signal of cases (a), (b), (c) and (d).

Parameter	Case	Value	Prior
Lens parameter			
Lens mass M_L	(a)	$1.53 \times 10^{12} M_\odot$	$U(10^9, 10^{13}) M_\odot$
	(c)	$1.53 \times 10^{10} M_\odot$	
Velocity dispersion v_d	(b)	405.5 km/s	$U(40, 1200)$ km/s
	(d)	128.2 km/s	
Lens redshift z_L		0.5	-
GW source position η_L		5 kpc	$U(0, 10)$ kpc
GW source parameter			
Deviation parameter η_0		0	$U(-1, 1)$
Source redshift z_S		1	-
Symmetric mass ratio η		0.222	$U(-1, 1)$
Inclination angle ι		$\pi/3$	$U(0, 1)$
Coalescence time t_c	2^{18}	s(~ 3 days)	$U(10^5, 10^6)$ s
Coalescence phase ϕ_c		$\pi/2$	$U(-\pi, \pi)$
Ecliptic latitude β		25.3°	-
Ecliptic longitude λ		120.4°	-
Polarization angle ψ_S		$\pi/2$	$U(0, \pi)$

IV. RESULTS

In order to verify the feasibility of the new method for testing CDDR using SLGW signals, we present the expected measurement precision of the deviation parameter η_0 for CDDR, based on simulated SLGW signals and the instrument specifications of the space-based GW detector, TianQin. The simulated GW source in this paper is MBBH. In this paper, we have considered different cases to compare the measurement precision of the deviation parameter η_0 , i.e. (a) PM model with $y = 0.3$, (b) SIS model with $y = 0.3$, (c) PM model with $y = 3.0$, and (d) SIS model with $y = 3.0$, different lens models with vary lens masses or velocity dispersions.

Given the parameter value (see Table I), the SLGW signals can be simulated according to Eq. (13), as shown in Figure 1. The vertical axis in Figure 1 represents the dimensionless GW characteristic strain $h_c = f \tilde{h}^L(f)$. The upper left corner corresponds to the case (a) PM model with $y = 0.3$; The upper right corner corresponds to the case (b) SIS model with $y = 0.3$; The lower left corner corresponds to the case (c) PM model with $y = 3.0$; The lower right corner corresponds to the case (d) SIS model with $y = 3.0$. The black solid line in the figure represents the unlensed GW signal, while the red dashed line and blue dotted line correspond to the lensed GW signal of μ_+ and μ_- , respectively. The green dashdot line represents the SLGW signal, as described in Eq. (13). Note that for the case (d) SIS model with $y \geq 1$, the SLGW signal has only one image of μ_+ . Due to $\eta_0 = 0$, the two parameterized forms $\eta_1(z)$ and $\eta_2(z)$ of $\eta(z)$ simulate the same SLGW signals.

In order to measure the deviation parameter η_0 of CDDR using SLGW signals, it is necessary to assume that the redshift of the source and lens is known, that is, an EM counterpart of the GW source and lens is required. By the way, the redshift mentioned in this article is the cosmological redshift and does not take into account the Doppler redshift of the GW source. Meanwhile, in order to simplify the calculation, we also fixed the position parameters β and λ of the GW source. Because it is assumed that there is an EM counterpart of the GW source, this operation is reasonable. This paper uses the two methods introduced in Section III, the FIM, and MCMC, to calculate the parameter estimation of SLGW signals.

The parameter estimation of SLGW signals with four cases (a), (b), (c), and (d) was performed using the FIM, and the measurement precision of the deviation parameter η_0 of the CDDR was obtained as listed in Table II. For the case (a), the measurement precision of η_0 is 0.9% in the parameterized form $\eta_1(z)$, and 1.9% in $\eta_2(z)$. For the case (b), the measurement precision of η_0 is 0.5% in the parameterized form $\eta_1(z)$, and 1.1% in $\eta_2(z)$. For the case (c), the measurement precision of η_0 is 1.3% in the parameterized form $\eta_1(z)$, and 2.6% in $\eta_2(z)$. For the case (d), regardless of whether the parameterized form $\eta_1(z)$ or $\eta_2(z)$ is used, the measurement precision of η_0 cannot be obtained. This is because the SIS model has only one image with GOA when $y \geq 1$, and in principle, it cannot recognize the SLGW signals in this case, thus unable to measure η_0 .

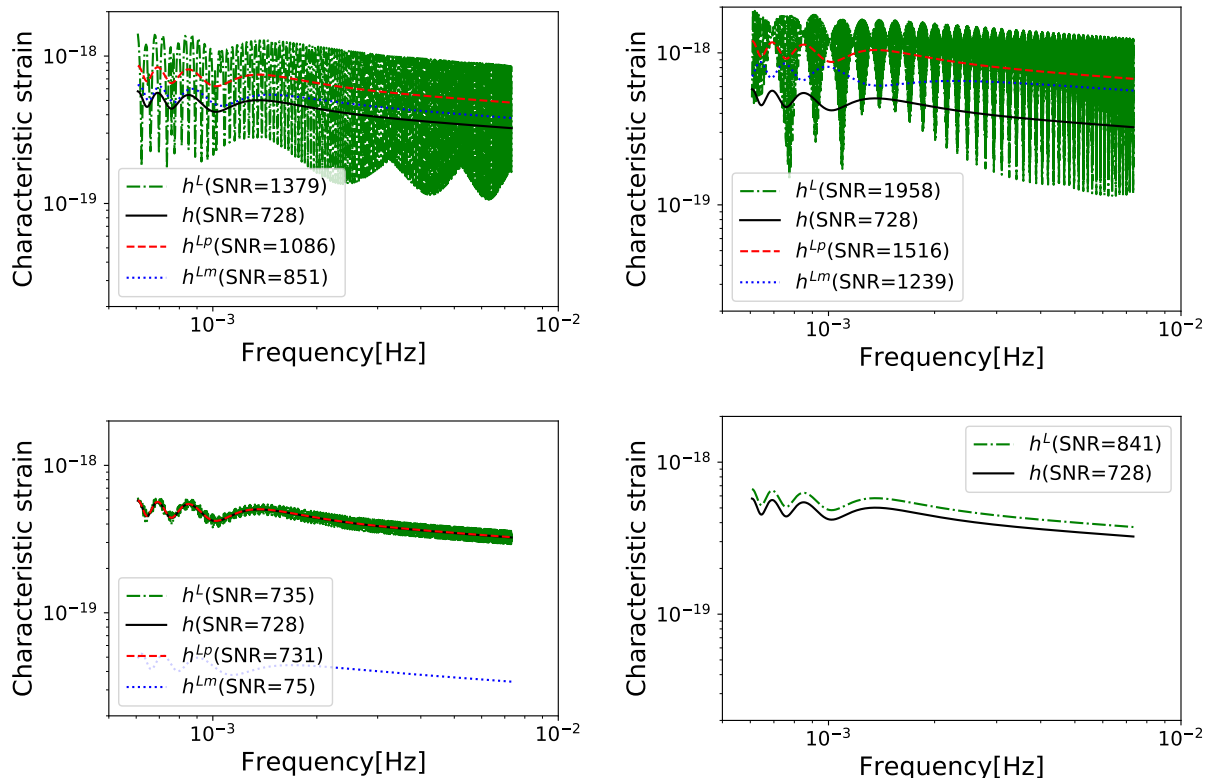


FIG. 1. Characteristic strain $h_c = f\tilde{h}^L(f)$ of SLGW signals for four cases: The upper left corner corresponds to the case (a) PM model with $y = 0.3$; The upper right corner corresponds to the case (b) SIS model with $y = 0.3$; The lower left corner corresponds to the case (c) PM model with $y = 3.0$; The lower right corner corresponds to the case (d) SIS model with $y = 3.0$. The black solid line in the figure represents the unlensed GW signal, while the red dashed line and blue dotted line correspond to the lensed GW signal of μ_+ and μ_- , respectively. The green dashdot line represents the SLGW signal, as described in Eq. (13). Note that for the case (d) SIS model with $y \geq 1$, the SLGW signal has only one image of μ_+ .

TABLE II. The measurement precision of η_0 .

Case	$\eta_1(z)$	$\eta_2(z)$
(a)PM, $y = 0.3$	± 0.009	± 0.019
(b)SIS, $y = 0.3$	± 0.005	± 0.011
(c)PM, $y = 3.0$	± 0.013	± 0.026
(d)SIS, $y = 3.0$	-	-

Assuming that the measurement of the deviation parameter η_0 follows a normal distribution. Using $\eta_0 = 0$ as the mean and the measurement precision of η_0 listed in Table II as the standard deviation, the probability density functions of η_0 can be drawn, as shown in Figure 2. The left panel shows the probability density functions of η_0 for cases (a) and (b) with $y = 0.3$. The blue dashdot and dotted lines correspond to the probability density functions of η_0 in the parameterized forms $\eta_1(z)$ and $\eta_2(z)$ of the case (a), while the red solid and dashed lines correspond to the probability density functions of η_0 in the parameterized forms $\eta_1(z)$ and $\eta_2(z)$ of the case (b). The right panel shows the probability density functions of η_0 for cases (c) and (d) with $y = 3.0$. The blue dashdot and dotted lines correspond to the probability density functions of η_0 in the parameterized forms $\eta_1(z)$ and $\eta_2(z)$ of the case (c). In the same probability density functions plot, a distribution that is higher and narrower indicates a higher measurement precision, while a distribution that is shorter and wider indicates a lower measurement precision.

$\eta_1(z)$ vs $\eta_2(z)$: By comparing the measurement precision of η_0 in the right two columns of Table II, or observing Figure 2, it can be found that for the same case, the parameterized form $\eta_1(z)$ has a better measurement precision of η_0 than $\eta_2(z)$. This is determined by the algebraic characteristics of these two parameterized forms, and the parameterized

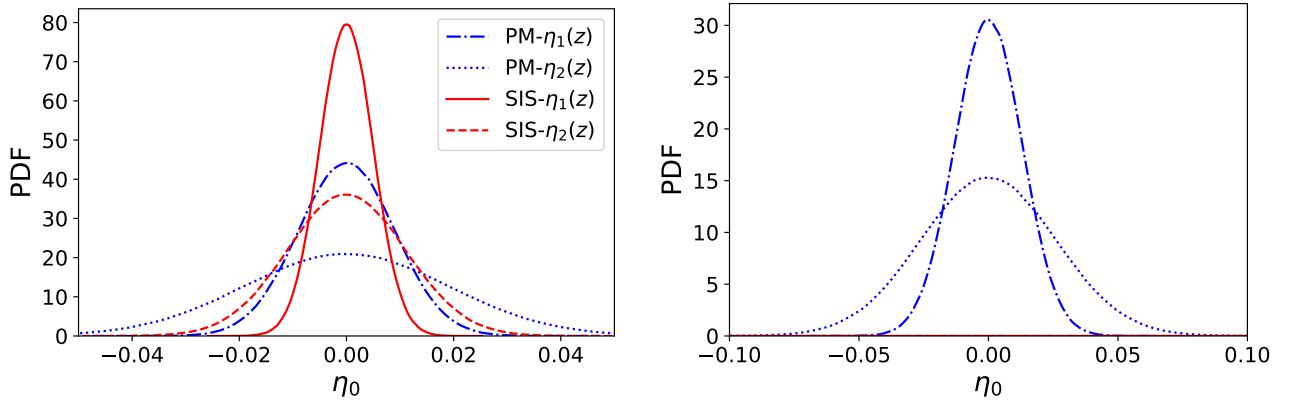


FIG. 2. The probability density functions of η_0 constrained by the SLGW signal with two parametric forms: $\eta_1(z) = 1 + \eta_0 z$ and $\eta_2(z) = 1 + \eta_0 z / (1 + z)$. Left panel: for cases (a) and (b) with $y = 0.3$; Right panel: for cases (c) and (d) with $y = 3$.

form $\eta_1(z)$ is more sensitive to changes in η_0 compared to $\eta_2(z)$. Specifically, the measurement precision of η_0 for $\eta_1(z)$ is almost half of that for $\eta_2(z)$. This is because, in this paper, when the redshift of the GW source is $z_S = 1$, the deviation term in $\eta_2(z) = 1 + \eta_0 z / (1 + z)$, $\eta_0 z / (1 + z)$, is half of the deviation term in $\eta_1(z) = 1 + \eta_0 z$, which is $\eta_0 z$ multiplied by $1 / (1 + z) = 1/2$. Similarly, if the redshift of the GW source is taken as $z_S = 2$, then the measurement precision of η_0 for $\eta_1(z)$ is almost one-third of that for $\eta_2(z)$, which is $1 / (1 + z) = 1/3$ times that of $\eta_2(z)$.

PM vs SIS: By comparing the second and third rows of Table II, or examining the left plot of Figure 2, it can be found that when y and the parameterized form $\eta(z)$ are the same, the SIS model has a better measurement precision of η_0 than the PM model. This is because at the same parameters value, the gravitational lensing effect for the SIS model is stronger than that for the PM model, that is, the magnification factor of the gravitational lensing calculated according to Eq. 10 is greater than that calculated by Eq. 8. Therefore, in the first row of Figure 1, the SNR of the SLGW for the SIS model is higher at 1958, while the SNR of the PM model is 1379.

$y = 0.3$ vs $y = 3.0$: By comparing the second and fourth rows of Table II, or comparing the two subgraphs in Figure 2, it can be found that for the same gravitational lens model, the measurement precision of η_0 is better for $y = 0.3$ compared to when $y = 3.0$. This is because as y decreases, the gravitational lens effect becomes more significant, resulting in an improvement in the measurement precision of η_0 .

Using the FIM calculation, the contour maps of the measurement precision of η_0 in the parameterized form $\eta_1(z)$ are shown in Figure 3 with the two-dimensional parameter space of the chirp mass and GW source redshift for both the PM model and the SIS model. The contour map of the PM model is shown on the left panel of Figure 3, while the SIS model is shown on the right panel. The white region in the right panel corresponds to the area where $y \geq 1$ in the SIS model. From Figure 3, it can be seen that both the contour maps of the PM model and the SIS model exhibit a symmetrical distribution about the chirp mass $\log_{10}(\mathcal{M}_z) = 5.3 M_\odot$. At the same redshift, the closer the chirp mass is to $\log_{10}(\mathcal{M}_z) = 5.3 M_\odot$, the higher the measurement precision of η_0 . As the redshift changes, the contour map shows oscillatory shapes. The characteristics of these contour maps in Figure 3 are related to two factors: the SNR of the SLGW signal and the amplification factor of the gravitational lensing effect.

On the one hand, the measurement precision of η_0 is related to the SNR of SLGW. The contour maps of SNR for GW signals are shown in Figure 4, where the upper left panel shows the SNR contour map for SLGW signals with the PM model, the upper right panel shows the SNR contour map for SLGW signals with the SIS model, and the lower panel shows the SNR contour map for unlensed GW signals. All panels show a peak around a small redshift z_S and $\log_{10}(\mathcal{M}_z) = 5.3 M_\odot$. Firstly, the smaller the GW source redshift z_S , the larger the GW amplitude as can be seen in Eq. (13), hence the higher the SNR. Secondly, at the same redshift, the GW source with a chirp mass of $\log_{10}(\mathcal{M}_z) = 5.3 M_\odot$ has the highest SNR due to the sensitivity band of TianQin. This explains the symmetrical distribution in Figure 3 concerning the straight line of a chirped mass $\log_{10}(\mathcal{M}_z) = 5.3 M_\odot$, and the closer to this line, the better the measurement precision of η_0 . Therefore, the higher the SNR of SLGW, the better the measurement precision of η_0 . When the redshift and chirp masses are the same, the SNR of SLGW in the SIS model is higher than that in the PM model. As mentioned earlier, this is because the SIS model has a stronger gravitational lensing effect.

On the other hand, the measurement precision of η_0 is related to the amplification factor of the gravitational lensing effect. Taking the PM model as an example, the graph of y changing with the redshift z_S and the amplification factor changing with y is shown in Figure 5. As y is independent of the chirp mass \mathcal{M}_z , the left panel in Figure 5 shows

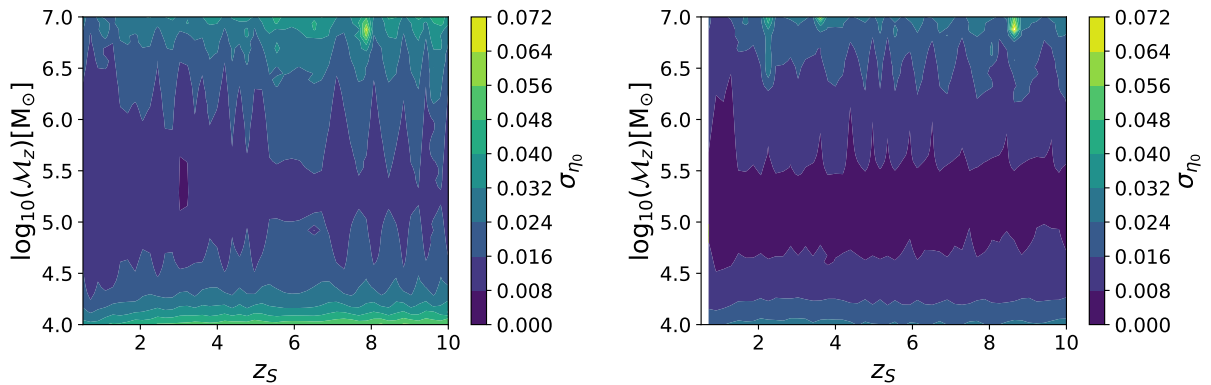


FIG. 3. The contour maps of the measurement precision of η_0 for both the PM model and the SIS model. Left panel: for the PM model; right panel: for the SIS model. The white region in the right panel corresponds to the area where $y \geq 1$ in the SIS model.

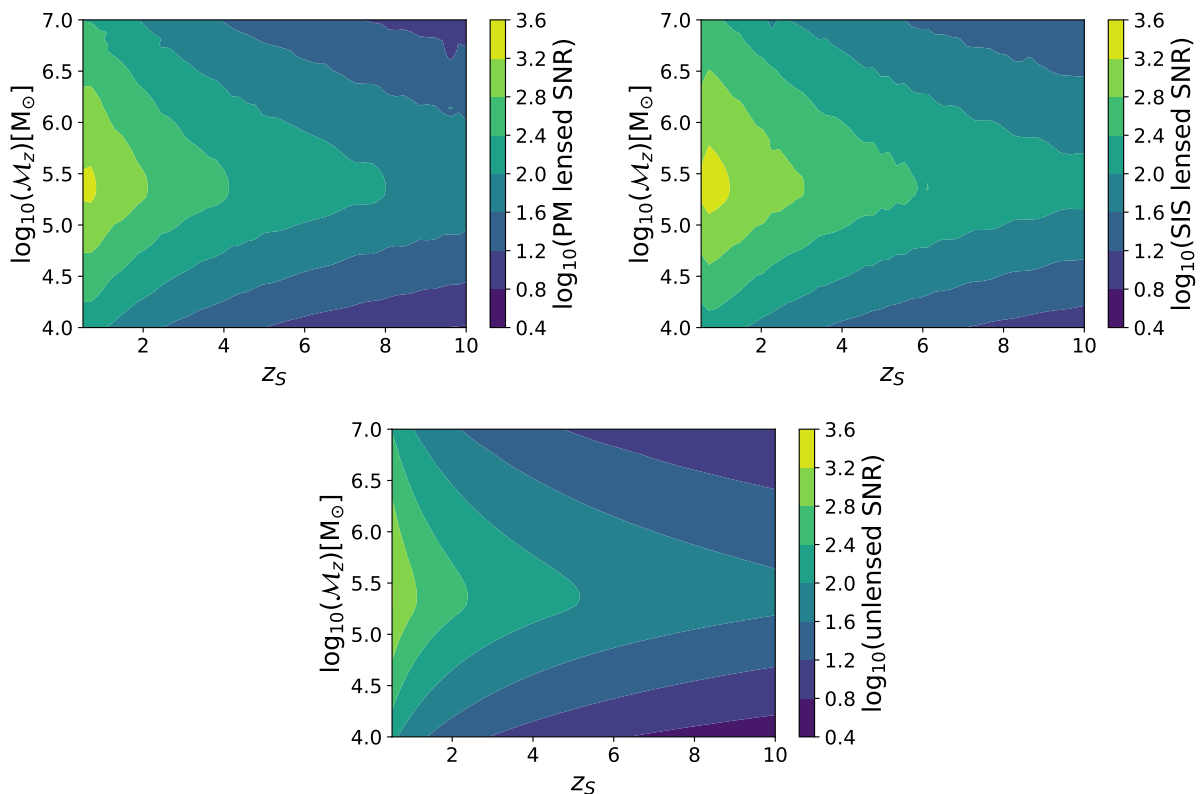


FIG. 4. The contour maps of SNR for GW signals. The upper left panel: the SNR contour map for SLGW signals with the PM model; the upper right panel: the SNR contour map for SLGW signals with the SIS model; the lower panel: the SNR contour map for unlensed GW signals.

that the value of y changes with the GW source redshift z_S . The right panel in Figure 5 shows that the magnitude of the amplification factor oscillates with the change of y . These can explain the oscillating structure in Figure 3.

When using MCMC sampling for parameter estimation, we can set the prior for the parameters shown in Table I. For case (c), the posterior distributions of the parameters in the parameterized forms $\eta_1(z)$ and $\eta_2(z)$ are shown in Figures 6 and 7, respectively. In these figures, the subplots on the diagonal show the histograms of the posterior distributions for each parameter, while the off-diagonal subplots show the two-dimensional density distribution of the 90% confidence intervals for each pair of parameters with a black line. The Gelman-Rubin statistic for all parameters' posterior distributions is less than 1.05, which means that the MCMC sampling has converged. For comparison, we

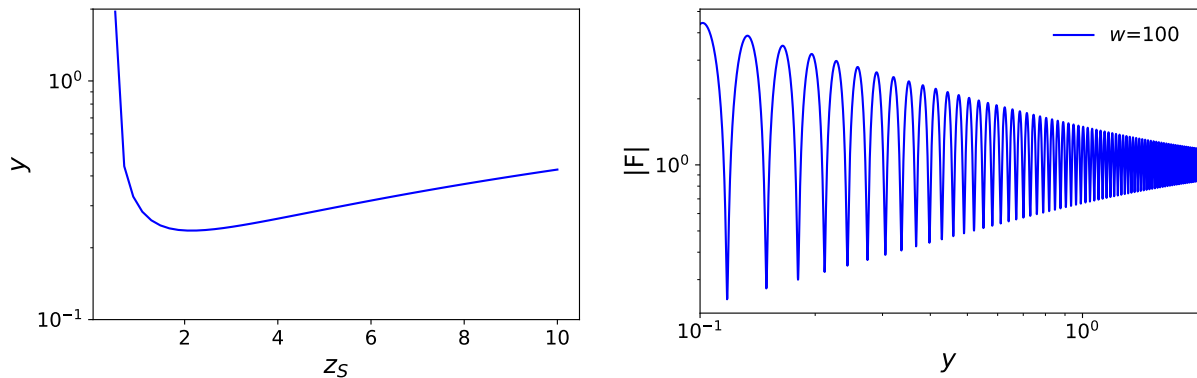


FIG. 5. The graph of y changing with the redshift z_s and the amplification factor $F_{geo}(w, y) = |\mu_+|^{1/2} - i|\mu_-|^{1/2} e^{i2\pi f t_d}$ changing with y in the PM model.

also cover the 90% confidence intervals calculated by the FIM in red ellipses in the same figures.

It can be found that both the FIM and MCMC sampling methods give consistent results for parameter estimation. The relative measurement errors of each parameter in the parameterized form η_1 can be obtained by Figure 6: $\sigma_{M_L}/M_L \approx 1.2\%$, $\sigma_{\eta_L}/\eta_L \approx 0.3\%$, $\sigma_{\mathcal{M}_z}/\mathcal{M}_z \approx 8.0 \times 10^{-5}$, $\sigma_\eta/\eta \approx 0.4\%$, $\sigma_{\cos \iota}/\cos \iota \approx 1.8\%$, $\sigma_{t_c}/t_c \approx 1.8 \times 10^{-6}$, $\sigma_{\phi_c}/\phi_c \approx 1.7\%$, and $\sigma_{\psi_S}/\psi_S \approx 0.2\%$; the absolute measurement error of η_0 is 1.3%. From Figure 7, it can be found that in the parameterized form η_2 , the relative measurement errors of each parameter are almost identical to those in η_1 , except for an increase in the absolute measurement error of η_0 to 2.6%.

V. SUMMARY AND DISCUSSION

This paper aimed to assess the viability of a novel method for testing the CDDR using SLGW signals. The investigation utilized simulated SLGW signals and the specifications of TianQin, focusing on a simulated GW source involving MBBHs. Four cases, namely (a) PM model with $y = 0.3$, (b) SIS model with $y = 0.3$, (c) PM model with $y = 3.0$, and (d) SIS model with $y = 3.0$, were considered to compare the measurement precision of the deviation parameter η_0 of CDDR.

The simulated SLGW signals were generated based on the parameters provided in Table I, and their waveforms are depicted in Figure 1. Parameterized forms $\eta_1(z)$ and $\eta_2(z)$ were employed to simulate SLGW signals corresponding to $\eta_0 = 0$. For testing CDDR using SLGW signals, the assumption of known source and lens redshifts and fixed position parameters of the GW source was made. Two methods, FIM and MCMC, were employed for the parameter estimation of SLGW signals.

The FIM-based parameter estimation, conducted for the four gravitational lens models, revealed the measurement precision of η_0 as listed in Table II. Case (a) exhibited a precision of 0.9% for $\eta_1(z)$ and 1.9% for $\eta_2(z)$, while case (b) showed 0.5% for $\eta_1(z)$ and 1.1% for $\eta_2(z)$. For case (c), the precision was 1.3% for $\eta_1(z)$ and 2.6% for $\eta_2(z)$. However, case (d) could not obtain the precision of η_0 due to the single image issue. Assuming a normal distribution for η_0 measurements, probability density functions were plotted, demonstrating that $\eta_1(z)$ generally exhibited better measurement precision than $\eta_2(z)$. Furthermore, comparisons were made for different lens models and y values, highlighting the impact on precision. The study delved into the relation between measurement precision of η_0 and SNR of SLGW signals, emphasizing the importance of source redshift and chirp mass. It was observed that a higher SNR corresponded to better measurement precision. Additionally, the effect of the amplification factor in gravitational lensing was discussed.

The consistency of parameter estimation methods between FIM and MCMC was established. For instance, in the case (c), the relative measurement errors for parameters in $\eta_1(z)$ were approximately 1.2% for M_L , 0.3% for η_L , 8.0×10^{-5} for \mathcal{M}_z , 0.4% for η , 1.8% for $\cos \iota$, 1.8×10^{-6} for t_c , 1.7% for ϕ_c , and 0.2% for ψ_S , resulting in an absolute measurement error of 1.3% for η_0 . In $\eta_2(z)$ case, the absolute measurement error of η_0 increased to 2.6%.

Overall, this investigation provided a comprehensive analysis of the proposed method's potential for testing CDDR using SLGW signals, taking into account various models and parameters. The results indicate that the method holds promise for precision measurements on η_0 , particularly when employing certain parameterized forms and gravitational lens models.

In this paper, some assumptions and simplifications were adopted to evaluate the proposed new method of testing

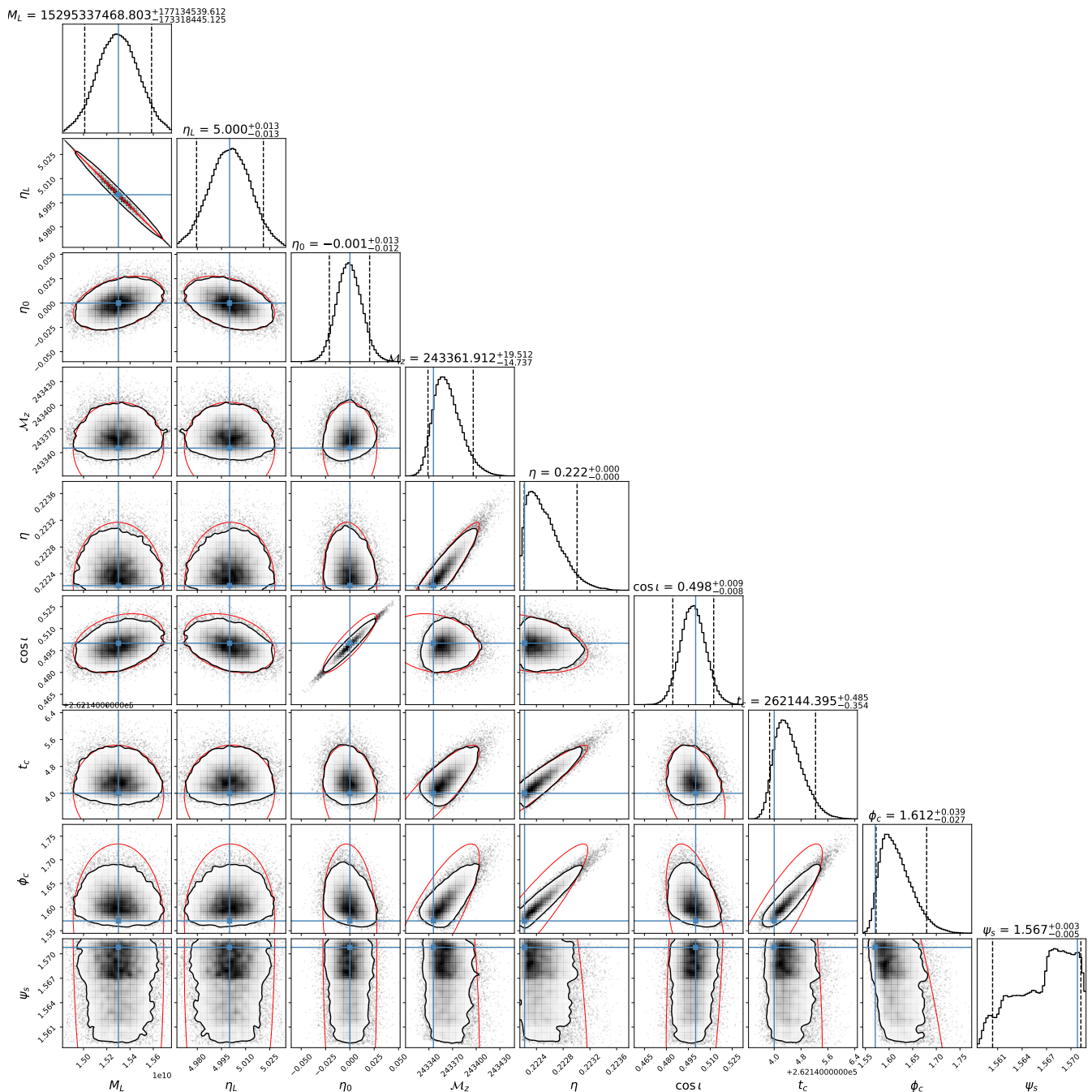


FIG. 6. The posterior distributions of the parameters in the parameterized form $\eta_1(z)$ for case (c) PM model with $y = 3.0$.

CDDR using SLGW signals. Firstly, we only calculate the SLGW using the gravitational lens models of PM and SIS, which are applicable to compact objects, stars, galaxies, galaxy clusters, and dark matter halos. In the future, we can further extend the gravitational lens models, including more complex models such as the NFW model [82, 83]. Secondly, the SLGW waveform used in this paper was given by the GOA. Although the GOA is still valid for the parameter range selected in this paper, the wave optics effect needs to be considered for more general cases [74]. Last but not least, in order to save computation time and improve efficiency, we used a PN expansion waveform that describes the quasi-circular orbit and no-spin binary star inspiral phase when calculating the SLGW signals from the merger of MBBH. Although this operation can greatly save computation time, the omission of the merger and ringdown phases means that the information of the GW signal is not fully utilized. In the future, the IMRPhenom waveform [84] that includes the inspiral, merger, and ringdown phases is required to calculate the SLGW signals, so

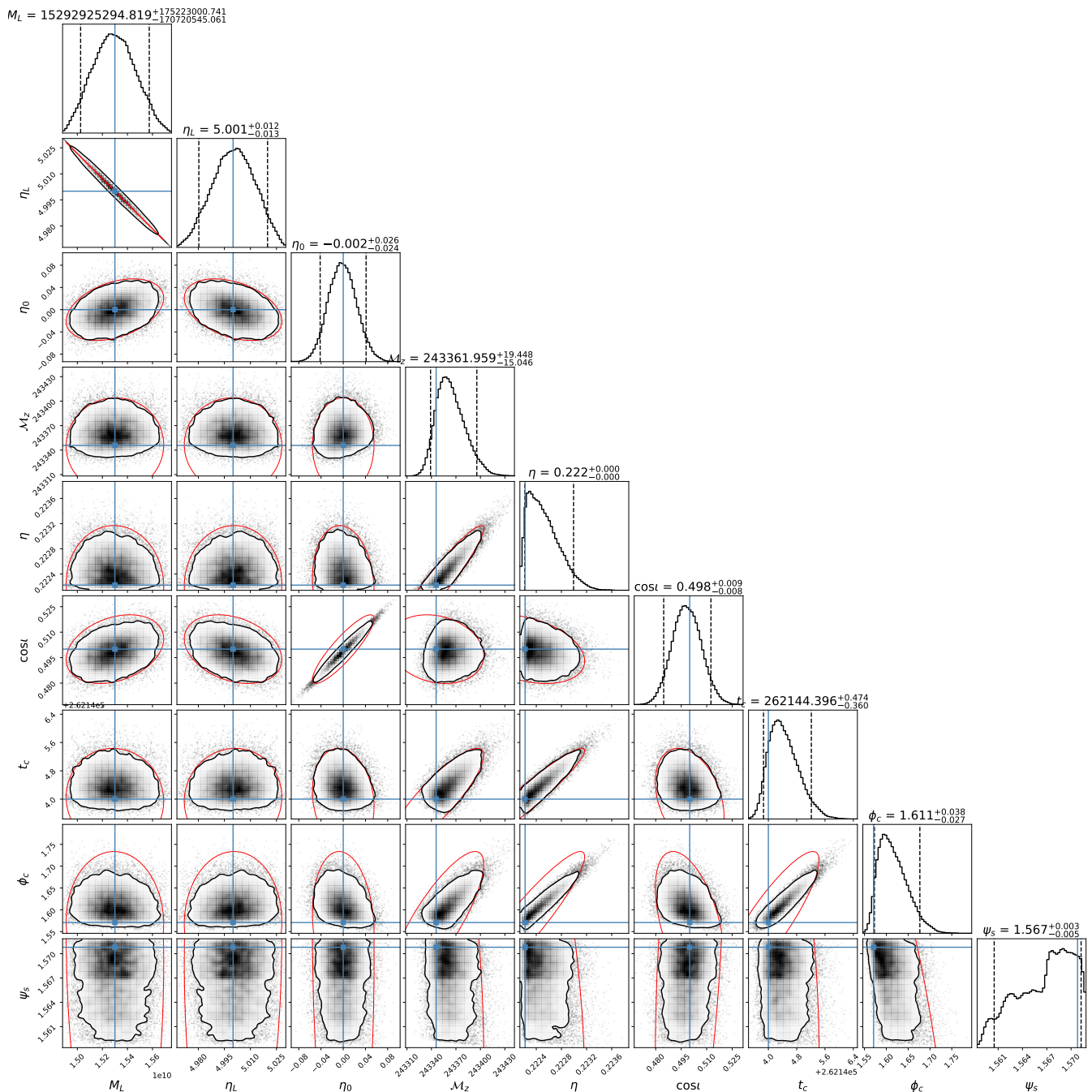


FIG. 7. The same as Figure 6, but in parameterized form $\eta_2(z)$.

that a more comprehensive analysis can be conducted. It is expected that using the IMRPhenom waveform can better constrain parameters including the deviation parameter η_0 of CDDR due to more information from the GW signal.

ACKNOWLEDGMENTS

This work was supported by the National Natural Science Foundation of China (Grants No. 12173104 and 12261131504), and Guangdong Major Project of Basic and Applied Basic Research (Grant No. 2019B030302001). E. K. L. was supported by the Natural Science Foundation of Guangdong Province of China (Grant No. 2022A1515011862).

Appendix A: Coordinate transformation

The transformation of the source position from the ecliptic coordinates (β, λ) to the detector coordinates (θ_S, ϕ_{S0}) for TianQin is described by the following formula:

$$\begin{pmatrix} d \sin \theta_S \cos \phi_{S0} \\ d \sin \theta_S \sin \phi_{S0} \\ d \cos \theta_S \end{pmatrix} = R_x(\theta = \beta' - 90^\circ) R_z(\theta = \lambda' - 90^\circ) \begin{pmatrix} d \cos \beta \cos \lambda \\ d \cos \beta \sin \lambda \\ d \sin \beta \end{pmatrix}, \quad (\text{A1})$$

where d is distance, and $\beta' = -4.7^\circ$, $\lambda' = 120^\circ$ are the ecliptic coordinates of TianQin's reference source, J0806. The rotation matrices are given by

$$R_x(\theta) = \begin{pmatrix} 1 & 0 & 0 \\ 0 & \cos \theta & \sin \theta \\ 0 & -\sin \theta & \cos \theta \end{pmatrix}, R_z(\theta) = \begin{pmatrix} \cos \theta & \sin \theta & 0 \\ -\sin \theta & \cos \theta & 0 \\ 0 & 0 & 1 \end{pmatrix}. \quad (\text{A2})$$

-
- [1] I. M. H. Etherington, *Philosophical Magazine* **15**, 761 (1933).
- [2] G. F. R. Ellis, *General Relativity and Gravitation* **39**, 1047 (2007).
- [3] B. A. Bassett and M. Kunz, *Phys. Rev. D* **69**, 101305 (2004), arXiv:astro-ph/0312443 [astro-ph].
- [4] P. S. Corasaniti, *MNRAS* **372**, 191 (2006), arXiv:astro-ph/0603833 [astro-ph].
- [5] G. F. R. Ellis, R. Poltis, J.-P. Uzan, and A. Weltman, *Phys. Rev. D* **87**, 103530 (2013), arXiv:1301.1312 [astro-ph.CO].
- [6] T. Liu, S. Cao, J. Zhang, M. Biesiada, Y. Liu, and Y. Lian, *MNRAS* **496**, 708 (2020), arXiv:2005.13990 [astro-ph.CO].
- [7] J.-Q. Xia, H. Yu, G.-J. Wang, S.-X. Tian, Z.-X. Li, S. Cao, and Z.-H. Zhu, *Astrophysical Journal* **834**, 75 (2017), arXiv:1611.04731 [astro-ph.CO].
- [8] J.-Z. Qi, S. Cao, S. Zhang, M. Biesiada, Y. Wu, and Z.-H. Zhu, *MNRAS* **483**, 1104 (2019), arXiv:1803.01990 [astro-ph.CO].
- [9] Planck Collaboration et al., *A&A* **641**, A6 (2020), arXiv:1807.06209 [astro-ph.CO].
- [10] S. Cao and Z. Zhu, *Science China Physics, Mechanics, and Astronomy* **54**, 2260 (2011), arXiv:1102.2750 [astro-ph.CO].
- [11] S. Cao, M. Biesiada, X. Zheng, and Z.-H. Zhu, *MNRAS* **457**, 281 (2016), arXiv:1601.00409 [astro-ph.CO].
- [12] R. F. L. Holanda, J. A. S. Lima, and M. B. Ribeiro, *A&A* **528**, L14 (2011), arXiv:1003.5906 [astro-ph.CO].
- [13] R. F. L. Holanda, J. A. S. Lima, and M. B. Ribeiro, *Astrophysical Journal* **722**, L233 (2010), arXiv:1005.4458 [astro-ph.CO].
- [14] Z. Li, P. Wu, and H. Yu, *Astrophysical Journal* **729**, L14 (2011), arXiv:1101.5255 [astro-ph.CO].
- [15] N. Liang, Z. Li, P. Wu, S. Cao, K. Liao, and Z.-H. Zhu, *MNRAS* **436**, 1017 (2013), arXiv:1104.2497 [astro-ph.CO].
- [16] F. S. Lima, R. F. L. Holanda, S. H. Pereira, and W. J. C. da Silva, *JCAP* **2021**, 035 (2021), arXiv:2104.06202 [astro-ph.CO].
- [17] P. Wu, Z. Li, X. Liu, and H. Yu, *Phys. Rev. D* **92**, 023520 (2015).
- [18] C.-Z. Ruan, F. Melia, and T.-J. Zhang, *Astrophysical Journal* **866**, 31 (2018), arXiv:1808.09331 [astro-ph.CO].
- [19] K. Liao, M. Biesiada, and Z.-H. Zhu, *Chinese Physics Letters* **39**, 119801 (2022), arXiv:2207.13489 [astro-ph.HE].
- [20] X. Li and H.-N. Lin, *MNRAS* **474**, 313 (2018), arXiv:1710.11361 [astro-ph.CO].
- [21] B. Xu, Z. Wang, K. Zhang, Q. Huang, and J. Zhang, *Astrophysical Journal* **939**, 115 (2022), arXiv:2212.00269 [astro-ph.CO].
- [22] K. Liao, Z. Li, S. Cao, M. Biesiada, X. Zheng, and Z.-H. Zhu, *Astrophysical Journal* **822**, 74 (2016), arXiv:1511.01318 [astro-ph.CO].
- [23] L. Tang, H.-N. Lin, and L. Liu, *Chinese Physics C* **47**, 015101 (2023), arXiv:2210.04228 [astro-ph.CO].
- [24] T. Liu, S. Cao, S. Ma, Y. Liu, C. Zheng, and J. Wang, arXiv e-prints, arXiv:2301.02997 (2023), arXiv:2301.02997 [astro-ph.CO].
- [25] H.-N. Lin and X. Li, *Chinese Physics C* **44**, 075101 (2020), arXiv:1911.00263 [gr-qc].
- [26] H.-N. Lin, X. Li, and L. Tang, *Chinese Physics C* **45**, 015109 (2021), arXiv:2010.03754 [gr-qc].
- [27] R. Arjona, H.-N. Lin, S. Nesseris, and L. Tang, *Phys. Rev. D* **103**, 103513 (2021), arXiv:2011.02718 [astro-ph.CO].
- [28] A. Avgoustidis, C. Burrage, J. Redondo, L. Verde, and R. Jimenez, *JCAP* **2010**, 024 (2010), arXiv:1004.2053 [astro-ph.CO].
- [29] Z. Li, P. Wu, H. Yu, and Z.-H. Zhu, *Phys. Rev. D* **87**, 103013 (2013).
- [30] K. Liao, A. Avgoustidis, and Z. Li, *Phys. Rev. D* **92**, 123539 (2015), arXiv:1512.01861 [astro-ph.CO].
- [31] X. Li, L. Tang, and H.-N. Lin, *MNRAS* **482**, 5678 (2019), arXiv:1707.00390 [gr-qc].
- [32] B. P. Abbott and others (LIGO Scientific Collaboration and Virgo Collaboration), *Physical Review X* **9**, 031040 (2019), arXiv:1811.12907 [astro-ph.HE].
- [33] R. Abbott and others (LIGO Scientific Collaboration and Virgo Collaboration), *Physical Review X* **11**, 021053 (2021), arXiv:2010.14527 [gr-qc].
- [34] R. Abbott and others (LIGO Scientific Collaboration and Virgo Collaboration), *Astrophysical Journal* **915**, L5 (2021), arXiv:2106.15163 [astro-ph.HE].

- [35] R. Abbott and others (LIGO Scientific Collaboration and Virgo Collaboration), arXiv e-prints , arXiv:2108.01045 (2021), [arXiv:2108.01045 \[gr-qc\]](#).
- [36] R. Abbott and others (LIGO Scientific Collaboration and Virgo Collaboration), arXiv e-prints , arXiv:2111.03606 (2021), [arXiv:2111.03606 \[gr-qc\]](#).
- [37] B. P. Abbott and others (LIGO Scientific Collaboration and Virgo Collaboration), *Phys. Rev. Lett.* **116**, 061102 (2016).
- [38] B. P. Abbott and others (LIGO Scientific Collaboration and Virgo Collaboration), *Phys. Rev. Lett.* **119**, 161101 (2017).
- [39] M. Sereno, A. Sesana, A. Bleuler, P. Jetzer, M. Volonteri, and M. C. Begelman, *Phys. Rev. Lett* **105**, 251101 (2010), [arXiv:1011.5238 \[astro-ph.CO\]](#).
- [40] Z. Gao, X. Chen, Y.-M. Hu, J.-D. Zhang, and S.-J. Huang, *MNRAS* **512**, 1 (2022), [arXiv:2102.10295 \[astro-ph.CO\]](#).
- [41] J. Luo and others (TianQin Collaboration), *Classical and Quantum Gravity* **33**, 035010 (2016), [arXiv:1512.02076 \[astro-ph.IM\]](#).
- [42] Y. M. Hu, J. Mei, and J. Luo, *National Science Review* **4**, 683 (2017).
- [43] W.-F. Feng, H.-T. Wang, X.-C. Hu, Y.-M. Hu, and Y. Wang, *Phys. Rev. D* **99**, 123002 (2019), [arXiv:1901.02159 \[astro-ph.IM\]](#).
- [44] J. Bao, C. Shi, H. Wang, J.-d. Zhang, Y. Hu, J. Mei, and J. Luo, *Phys. Rev. D* **100**, 084024 (2019), [arXiv:1905.11674 \[gr-qc\]](#).
- [45] C. Shi, J. Bao, H. Wang, J.-d. Zhang, Y. Hu, A. Sesana, E. Barausse, J. Mei, and J. Luo, *Phys. Rev. D* **100**, 044036 (2019), [arXiv:1902.08922 \[gr-qc\]](#).
- [46] H.-T. Wang, Z. Jiang, A. Sesana, E. Barausse, S.-J. Huang, Y.-F. Wang, W.-F. Feng, Y. Wang, Y.-M. Hu, J. Mei, and J. Luo, *Phys. Rev. D* **100**, 043003 (2019), [arXiv:1902.04423 \[astro-ph.HE\]](#).
- [47] S. Liu, Y.-M. Hu, J.-d. Zhang, and J. Mei, *Phys. Rev. D* **101**, 103027 (2020), [arXiv:2004.14242 \[astro-ph.HE\]](#).
- [48] H.-M. Fan, Y.-M. Hu, E. Barausse, A. Sesana, J.-d. Zhang, X. Zhang, T.-G. Zi, and J. Mei, *Phys. Rev. D* **102**, 063016 (2020), [arXiv:2005.08212 \[astro-ph.HE\]](#).
- [49] S.-J. Huang, Y.-M. Hu, V. Korol, P.-C. Li, Z.-C. Liang, Y. Lu, H.-T. Wang, S. Yu, and J. Mei, *Phys. Rev. D* **102**, 063021 (2020), [arXiv:2005.07889 \[astro-ph.HE\]](#).
- [50] J. Mei and others (TianQin Collaboration), *Progress of Theoretical and Experimental Physics* **2021**, 05A107 (2021), [arXiv:2008.10332 \[gr-qc\]](#).
- [51] T. Zi, J.-d. Zhang, H.-M. Fan, X.-T. Zhang, Y.-M. Hu, C. Shi, and J. Mei, *Phys. Rev. D* **104**, 064008 (2021), [arXiv:2104.06047 \[gr-qc\]](#).
- [52] Z.-C. Liang, Y.-M. Hu, Y. Jiang, J. Cheng, J.-d. Zhang, and J. Mei, *Phys. Rev. D* **105**, 022001 (2022), [arXiv:2107.08643 \[astro-ph.CO\]](#).
- [53] S. Liu, L.-G. Zhu, Y.-M. Hu, J.-d. Zhang, and M.-J. Ji, *Phys. Rev. D* **105**, 023019 (2022), [arXiv:2110.05248 \[astro-ph.HE\]](#).
- [54] L.-G. Zhu, L.-H. Xie, Y.-M. Hu, S. Liu, E.-K. Li, N. R. Napolitano, B.-T. Tang, J.-D. Zhang, and J. Mei, *Science China Physics, Mechanics, and Astronomy* **65**, 259811 (2022), [arXiv:2110.05224 \[astro-ph.CO\]](#).
- [55] L.-G. Zhu, Y.-M. Hu, H.-T. Wang, J.-d. Zhang, X.-D. Li, M. Hendry, and J. Mei, *Physical Review Research* **4**, 013247 (2022), [arXiv:2104.11956 \[astro-ph.CO\]](#).
- [56] X.-T. Zhang, C. Messenger, N. Korsakova, M. L. Chan, Y.-M. Hu, and J.-d. Zhang, *Phys. Rev. D* **105**, 123027 (2022), [arXiv:2202.07158 \[astro-ph.HE\]](#).
- [57] Y. Lu, E.-K. Li, Y.-M. Hu, J.-d. Zhang, and J. Mei, arXiv e-prints , arXiv:2205.02384 (2022), [arXiv:2205.02384 \[astro-ph.GA\]](#).
- [58] S. Sun, C. Shi, J.-d. Zhang, and J. Mei, arXiv e-prints , arXiv:2207.13009 (2022), [arXiv:2207.13009 \[gr-qc\]](#).
- [59] N. Xie, J.-d. Zhang, S.-J. Huang, Y.-M. Hu, and J. Mei, arXiv e-prints , arXiv:2208.10831 (2022), [arXiv:2208.10831 \[gr-qc\]](#).
- [60] J. Cheng, E.-K. Li, Y.-M. Hu, Z.-C. Liang, J.-d. Zhang, and J. Mei, *Phys. Rev. D* **106**, 124027 (2022), [arXiv:2208.11615 \[gr-qc\]](#).
- [61] H.-M. Fan, S. Zhong, Z.-C. Liang, Z. Wu, J.-d. Zhang, and Y.-M. Hu, *Phys. Rev. D* **106**, 124028 (2022), [arXiv:2209.13387 \[gr-qc\]](#).
- [62] C. Shi, M. Ji, J.-d. Zhang, and J. Mei, *Phys. Rev. D* **108**, 024030 (2023), [arXiv:2210.13006 \[gr-qc\]](#).
- [63] L. Ren, C. Li, B. Ma, S. Cheng, S.-J. Huang, B. Tang, and Y.-m. Hu, *ApJS* **264**, 39 (2023), [arXiv:2302.02802 \[astro-ph.SR\]](#).
- [64] Z.-C. Liang, Z.-Y. Li, E.-K. Li, J.-d. Zhang, and Y.-M. Hu, arXiv e-prints , arXiv:2307.01541 (2023), [arXiv:2307.01541 \[gr-qc\]](#).
- [65] S.-J. Huang, Y.-M. Hu, X. Chen, J.-d. Zhang, E.-K. Li, Z. Gao, and X.-y. Lin, *JCAP* **2023**, 003 (2023), [arXiv:2304.10435 \[astro-ph.CO\]](#).
- [66] X.-y. Lin, J.-d. Zhang, L. Dai, S.-J. Huang, and J. Mei, *Phys. Rev. D* **108**, 064020 (2023), [arXiv:2304.04800 \[gr-qc\]](#).
- [67] C.-Q. Ye, J.-H. Chen, J.-d. Zhang, H.-M. Fan, and Y.-M. Hu, *MNRAS* (2023), 10.1093/mnras/stad3296, [arXiv:2307.08231 \[astro-ph.HE\]](#).
- [68] X. Lyu, E.-K. Li, and Y.-M. Hu, *Phys. Rev. D* **108**, 083023 (2023), [arXiv:2307.12244 \[gr-qc\]](#).
- [69] A. Torres-Orjuela, S.-J. Huang, Z.-C. Liang, S. Liu, H.-T. Wang, C.-Q. Ye, Y.-M. Hu, and J. Mei, arXiv e-prints , [arXiv:2307.16628 \(2023\)](#), [arXiv:2307.16628 \[gr-qc\]](#).
- [70] H. Wang, I. Harry, A. Nitz, and Y.-M. Hu, arXiv e-prints , [arXiv:2304.10340 \(2023\)](#), [arXiv:2304.10340 \[astro-ph.HE\]](#).
- [71] H.-Y. Chen, X.-Y. Lyu, E.-K. Li, and Y.-M. Hu, arXiv e-prints , [arXiv:2309.06910 \(2023\)](#), [arXiv:2309.06910 \[gr-qc\]](#).
- [72] S. d'Ascoli, S. C. Noble, D. B. Bowen, M. Campanelli, J. H. Krolik, and V. Mewes, *Astrophysical Journal* **865**, 140 (2018), [arXiv:1806.05697 \[astro-ph.HE\]](#).
- [73] N. Tamanini, C. Caprini, E. Barausse, A. Sesana, A. Klein, and A. Petiteau, *JCAP* **2016**, 002 (2016), [arXiv:1601.07112 \[astro-ph.CO\]](#).

- [74] R. Takahashi and T. Nakamura, *Astrophysical Journal* **595**, 1039 (2003), arXiv:astro-ph/0305055 [astro-ph].
- [75] X. Yang, H.-R. Yu, Z.-S. Zhang, and T.-J. Zhang, *Astrophysical Journal* **777**, L24 (2013), arXiv:1310.0869 [astro-ph.CO].
- [76] R. F. L. Holanda, V. C. Busti, and J. S. Alcaniz, *JCAP* **2016**, 054 (2016), arXiv:1512.02486 [astro-ph.CO].
- [77] K. Liao, *Astrophysical Journal* **885**, 70 (2019), arXiv:1906.09588 [astro-ph.CO].
- [78] D. W. Hogg, *arXiv e-prints*, astro-ph/9905116 (1999), arXiv:astro-ph/9905116 [astro-ph].
- [79] L. S. Finn, *Phys. Rev. D* **46**, 5236 (1992), arXiv:gr-qc/9209010 [gr-qc].
- [80] C. Cutler and É. E. Flanagan, *Phys. Rev. D* **49**, 2658 (1994), arXiv:gr-qc/9402014 [gr-qc].
- [81] D. Foreman-Mackey, D. W. Hogg, D. Lang, and J. Goodman, *PASP* **125**, 306 (2013), arXiv:1202.3665 [astro-ph.IM].
- [82] J. F. Navarro, C. S. Frenk, and S. D. M. White, *Astrophysical Journal* **462**, 563 (1996), arXiv:astro-ph/9508025 [astro-ph].
- [83] J. F. Navarro, C. S. Frenk, and S. D. M. White, *Astrophysical Journal* **490**, 493 (1997), arXiv:astro-ph/9611107 [astro-ph].
- [84] S. Khan, F. Ohme, K. Chatziioannou, and M. Hammam, *Phys. Rev. D* **101**, 024056 (2020).